Hard-Rock Coherency Functions Based on the Pinyon Flat Array Data

Norman A. Abrahamson
Norman A. Abrahamson, Inc
Piedmont CA

Draft Report to EPRI
July 5, 2007

ACKNOWLEDGMENTS

This document describes research sponsored by the Electric Power Research Institute (EPRI) and the U.S. Department of Energy under Award No. (DE-FC07-04ID14533). Any opinions, findings, and conclusions or recommendations expressed in this material are those of the author(s) and do not necessarily reflect the views of the Department of Energy.

The Pinyon Flat Array data was compiled by Melanie Walling.

CONTENTS

LIST OF FIGURES

LIST OF TABLES

1 Introduction

In a previous study, Abrahamson (2006) presented coherency models for short separation distances (0-150m) based on surface recordings from a suite of dense arrays located in Taiwan, Japan, and California. Most of these arrays were located on soil or soft-rock sites. The applicability of these data to hard-rock conditions in the EUS has been discussed at review meetings with the NRC. Of the data considered in the previous study, the Pinyon Flat array, described below, is the only hard-rock site. In this report, a new coherency model is derived using only the recordings from the Pinyon Flat array. This data set leads to larger coherency at high frequencies than the model presented in Abrahamson (2006).

The Pinyon Flat array is located in Southern California between the San Jacinto and southern San Andreas Faults. The array was deployed as part of a PASSCAL experiment to study wave propagation, scattering, and spatial variations (Owens et al. 1991). The Pinyon Flat area consists of granite. A shear-wave velocity profile from down-hole measurements (Louie et al., 2002) is shown in Figure 1. The top layer is highly weathered. This layer was removed with a backhoe and the instruments were plastered to the rock at depth of 1-3 m below the ground surface. The rock is called "semi-competent rock" by Vernon et al. (1995) since it is still partially weathered at the top. Competent rock, with a shear-wave velocity of 880 m/s, is reached at a depth of 5 m (3 m below the instruments). The shear-wave velocity increases to 1600 m/s at a depth of 13 m. The average shear-wave velocity in the 30 m below the instrument embedment depth is 1030 m/s.

The Pinyon Flat array consists of 58 force-balanced accelerometers. The array has two parts. In one part, the instruments are configured in an L-Shaped array and in the second part 36 instruments are configured in a dense grid with 6-7 m spacing (Figure 2).

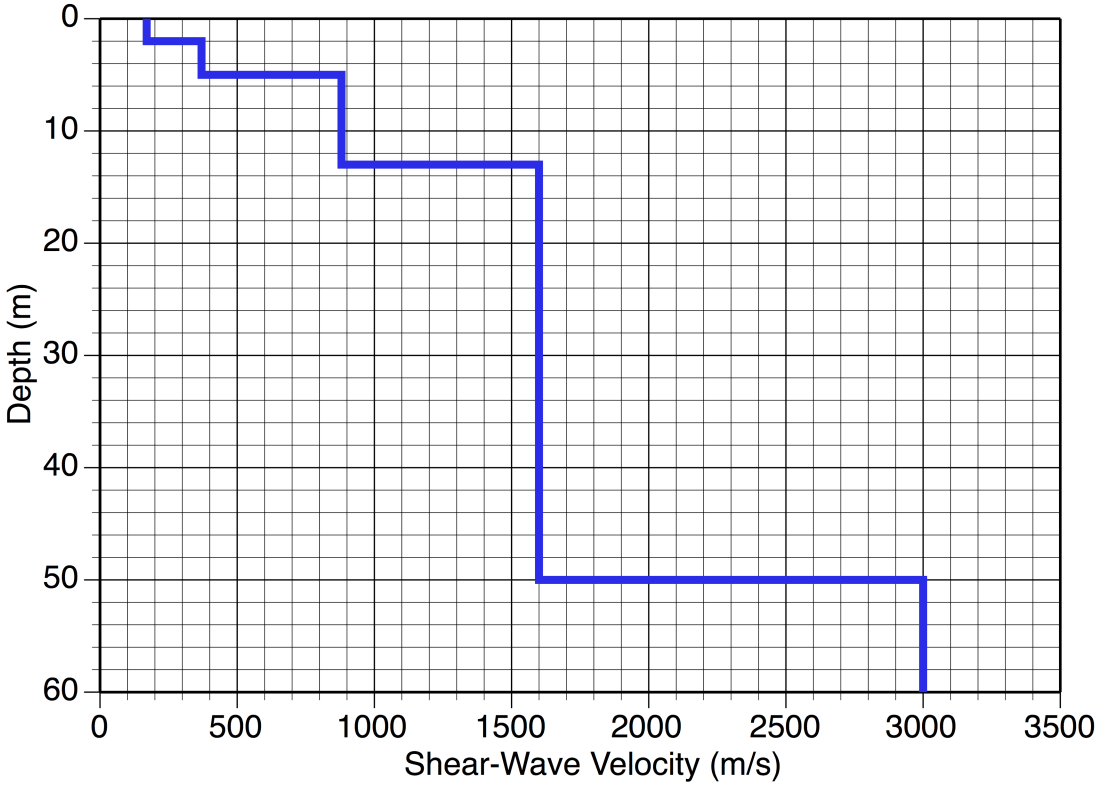

Figure 1. Shear-wave velocity profile at the Pinyon Flat array based on down-hole measurements.

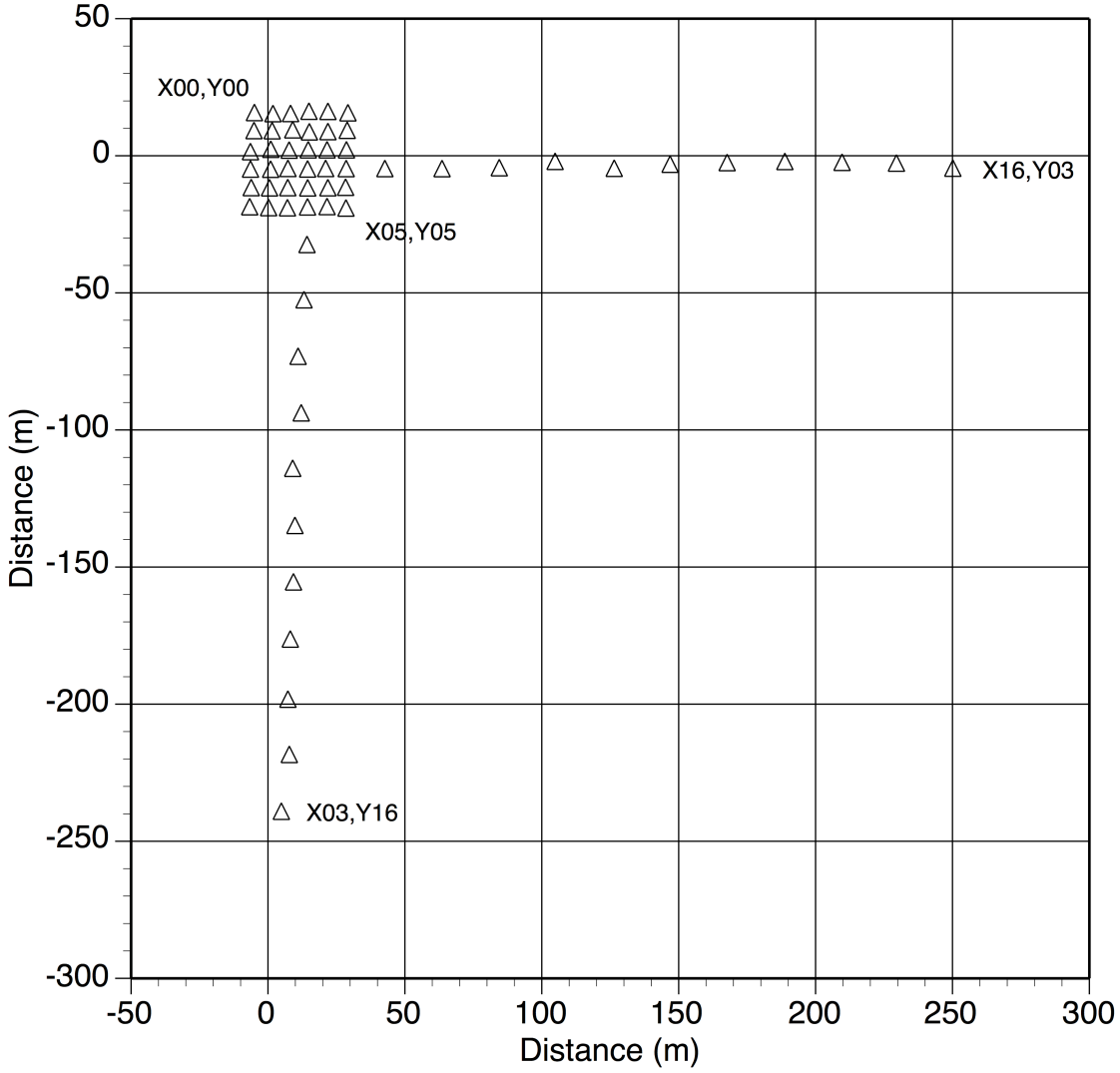

Figure 2. Configuration of the Pinyon Flat array

2 Data Set

From the 1990 deployment of the dense array at Pinyon Flat (Vernon et al., 1995), there are recordings from 287 earthquakes available through the IRIS data center. The earthquakes magnitudes are all less than 4 with most of these earthquakes from magnitudes less than 2.

2.1 TIME WINDOWS

The time windows were selected based on the duration of the normalized Arias intensity of the two horizontal components of velocity. The recordings can have long pre-event and post-event memory. Even though the ground motion is much lower in these sections of the records, if they are very long, they can have a significant effect on the normalized Arias intensity. Therefore, an initial data window was applied that starts 10 seconds before the peak velocity and ends 10 seconds after the peak velocity. (The peak velocity is defined as the largest velocity on either of the two horizontal components).

The normalized Arias intensity is then given by:

$$I(\tau) = \frac{\int_{T_P-10}^{\tau} V_1^2(t) + V_2^2(t)\,dt}{\int_{T_P-10}^{T_P+10} V_1^2(t) + V_2^2(t)\,dt} \qquad (2\text{-}1)$$

where T_p is the time of the peak velocity. A window based on the time at which the normalized Arias intensity reaches a value of 0.10 and 0.75. These times are denoted $T_{0.1}$ and $T_{0.75}$. To avoid a very short duration, the start time of the window is set 0.5 seconds before $T_{0.1}$ and 1.0 seconds after $T_{0.75}$. An example of the initial windowing is shown in Figure 3. The final window is based on the normalized Arias intensity. Examples of the final windows are shown in Figures 4 and 5 for short and long duration records, respectively.

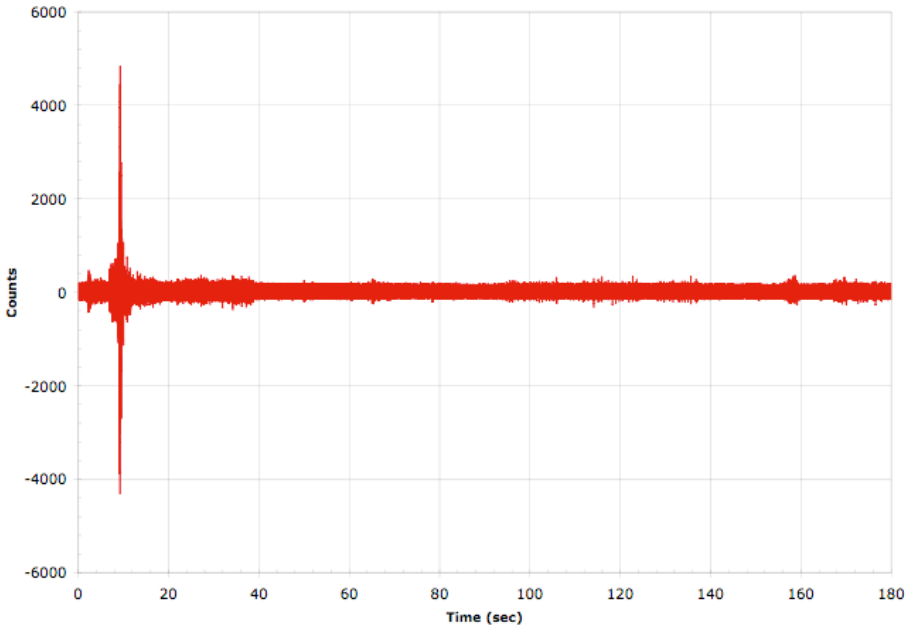

Figure 3. Example of the long post-event memory from a recording from the Pinyon Flat array (Event 90.108.01.16.51). The peak velocity is at 9.2 sec. An initial window from 0 to 19.2 sec is selected.

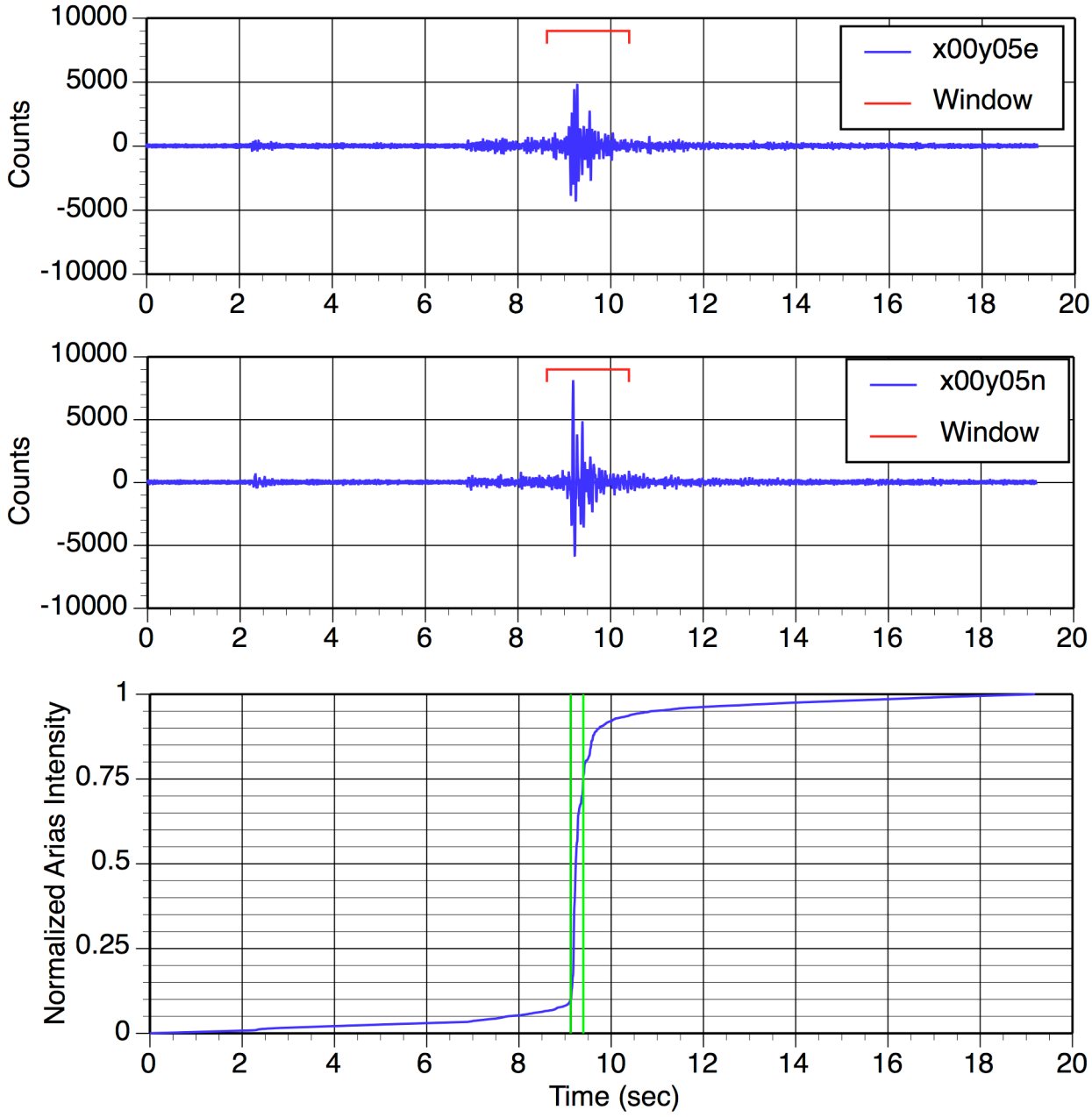

Figure 4. Example of the final window selected from the 20 seconds about the peak velocity for a short duration recording.

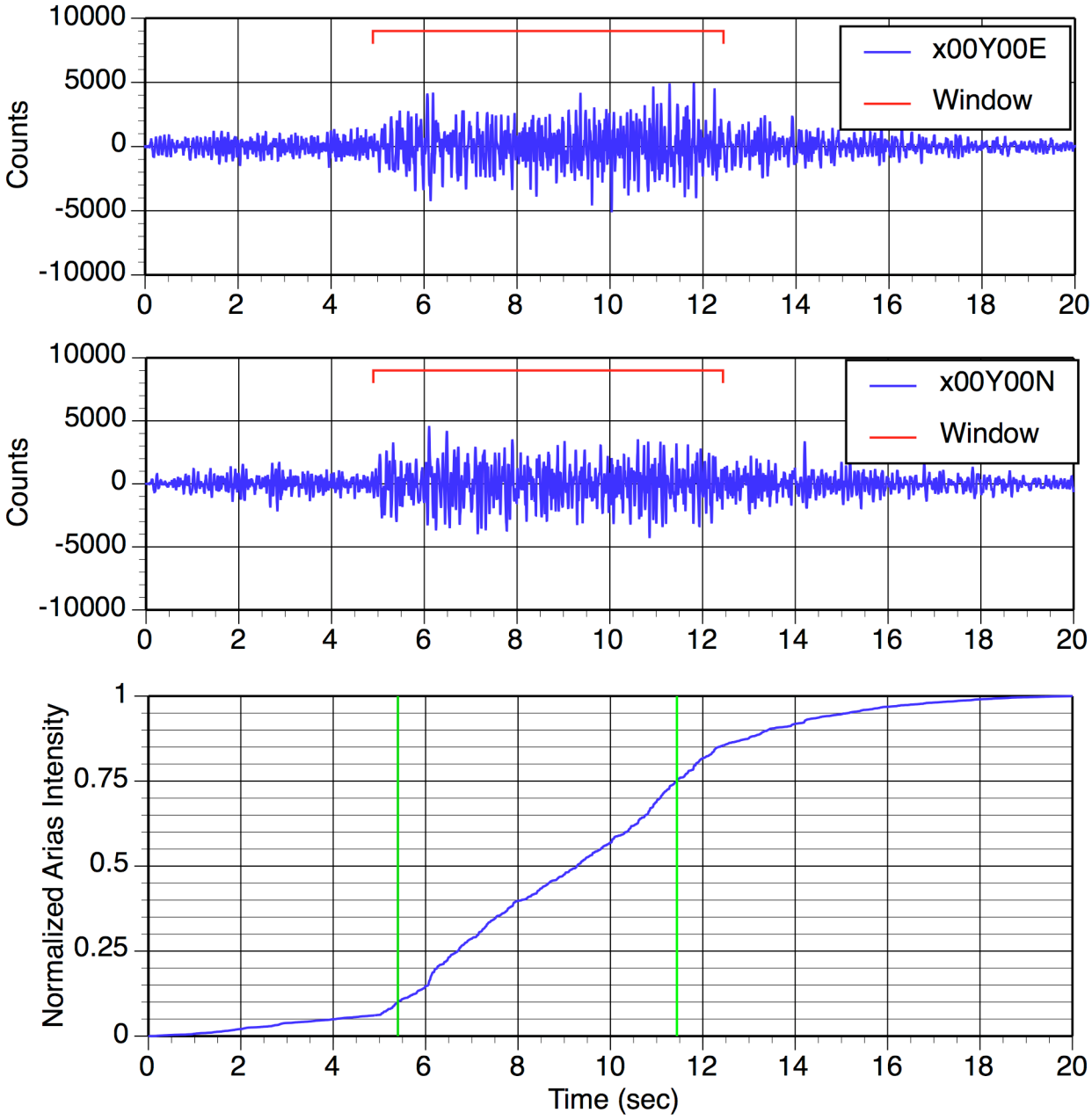

Figure 5. Example of the final window selected from the 20 seconds about the peak velocity for a long duration recording.

2.2 SUBSET OF SELECTED EARTHQUAKES

From the set of 287 earthquakes, a subset was selected based on the signal in the frequency range of 10 to 40 hz which is a key frequency range of the application of the coherency model for nuclear power plants. The mean Fourier spectrum of the windowed acceleration for each component is computed for each earthquake. Those earthquakes with good signal to noise in the frequency band 10-40 Hz were selected. The 78 selected earthquakes are listed in Table 1.

Table 1. Selected Earthquakes and Data Windows

Event Number	Event Name	Number of Stations	Start Time	Window Duration (sec)
1	90.108/90.108.01.16.51	8	13:36:00.846	1.764
2	90.108/90.108.10.23.27	40	07:58:58.746	7.540
3	90.108/90.108.14.25.58	40	05:06:14.818	7.628
4	90.108/90.108.14.32.41	40	11:56:27.469	6.716
5	90.108/90.108.19.07.21	51	11:30:15.057	8.024
6	90.109/90.109.05.43.34	51	08:54:21.877	8.120
7	90.109/90.109.08.42.55	51	08:25:18.353	2.120
8	90.109/90.109.20.24.52	51	14:32:24.349	7.320
9	90.110/90.110.02.24.45	51	14:26:17.505	1.816
10	90.110/90.110.03.24.54	51	12:33:59.529	5.324
11	90.110/90.110.07.21.01	49	07:15:52.521	5.552
12	90.110/90.110.17.48.02	49	13:36:37.817	7.548
13	90.111/90.111.17.29.03	49	13:29:46.001	7.472
26	90.115/90.115.03.29.27	53	19:02:40.329	1.728
29	90.115/90.115.07.08.28	51	21:48:44.069	2.980
30	90.115/90.115.07.10.58	51	14:23:46.857	7.264
32	90.115/90.115.09.46.24	53	10:15:21.149	1.808
33	90.115/90.115.09.53.30	53	03:54:20.505	7.324
39	90.115/90.115.16.26.39	51	13:32:12.040	1.744
44	90.115/90.115.22.36.37	51	03:08:12.520	3.904
61	90.117/90.117.13.51.16	47	12:15:03.040	12.208
63	90.117/90.117.15.40.10	43	11:30:30.764	4.592
65	90.117/90.117.20.03.12	43	00:22:54.168	6.844
67	90.118/90.118.08.32.30	51	18:50:42.016	7.916
68	90.118/90.118.10.12.04	51	18:44:36.160	2.104
69	90.118/90.118.14.23.11	51	17:02:59.220	6.896
71	90.118/90.118.15.21.32	49	06:28:56.476	6.524
74	90.119/90.119.02.56.08	47	23:16:27.188	2.128
76	90.119/90.119.11.25.57	43	17:04:19.980	1.892
80	90.119/90.119.19.35.48	41	21:42:06.416	8.176
84	90.120/90.120.06.01.41	39	13:46:54.624	1.800
85	90.120/90.120.06.56.22	39	07:42:46.368	1.760
86	90.120/90.120.07.30.46	39	07:16:10.076	4.960
88	90.120/90.120.20.16.54	39	02:29:07.328	4.568
100	90.122/90.122.14.13.10	51	16:19:58.200	3.864
125	90.127/90.127.07.58.05	36	01:36:52.728	1.944
126	90.127/90.127.12.41.00	36	00:57:47.536	7.344
128	90.127/90.127.21.01.53	36	22:13:29.828	5.328

Table 1. Selected Earthquakes and Data Windows (Cont.)

Event Number	Event Name	Number of Stations	Start Time	Window Duration (sec)
131	90.128/90.128.10.18.33	36	18:04:24.428	2.448
136	90.129/90.129.22.05.28	57	15:19:17.216	1.760
141	90.130/90.130.07.23.31	57	14:20:51.464	5.580
143	90.130/90.130.10.42.12	57	13:25:21.260	2.292
144	90.130/90.130.12.10.41	57	12:10:53.220	1.764
146	90.130/90.130.14.16.02	57	08:39:47.348	1.964
148	90.130/90.130.14.25.08	57	01:41:19.900	7.884
152	90.130/90.130.15.19.06	57	22:05:38.800	1.912
154	90.130/90.130.15.57.44	57	00:22:31.556	1.920
156	90.130/90.130.17.29.42	55	15:00:28.800	1.764
161	90.131/90.131.00.54.55	55	19:01:38.964	1.760
162	90.131/90.131.00.57.36	55	12:41:09.088	1.780
175	90.132/90.132.15.16.58	50	17:27:56.960	1.736
180	90.132/90.132.19.42.46	50	15:03:09.076	1.876
184	90.132/90.132.23.54.47	55	06:59:49.488	9.356
190	90.134/90.134.05.05.20	57	13:05:48.591	2.372
192	90.134/90.134.07.29.45	55	16:24:46.929	1.748
195	90.134/90.134.11.32.06	57	09:09:43.625	1.764
196	90.134/90.134.11.34.45	57	08:59:31.797	1.752
199	90.135/90.135.00.10.14	57	22:39:26.253	4.176
200	90.135/90.135.02.28.56	57	20:17:13.761	4.560
204	90.135/90.135.13.46.43	57	06:01:55.517	1.808
209	90.136/90.136.01.14.15	57	17:55:40.724	1.960
211	90.136/90.136.04.53.05	55	16:22:39.344	1.728
213	90.136/90.136.18.14.38	53	05:26:17.256	1.816
215	90.137/90.137.02.36.37	53	02:50:47.334	4.140
226	90.138/90.138.12.05.42	51	14:38:34.008	2.908
234	90.139/90.139.06.30.57	53	05:06:10.174	5.608
236	90.139/90.139.09.48.19	53	20:28:51.926	2.868
237	90.139/90.139.11.36.56	53	18:57:41.302	3.856
243	90.140/90.140.01.15.48	53	01:29:58.762	1.760
245	90.140/90.140.04.54.23	53	22:23:35.878	3.644
250	90.141/90.141.14.14.09	53	15:22:12.014	1.776
251	90.142/90.142.00.02.28	53	14:37:44.450	1.900
252	90.142/90.142.03.22.47	53	14:29:19.454	1.832
260	90.144/90.144.00.05.41	49	04:43:19.550	1.816
270	90.145/90.145.03.59.16	56	23:53:18.494	2.332
271	90.145/90.145.04.15.25	56	17:38:12.841	1.740
274	90.145/90.145.12.35.53	54	17:32:01.181	6.428
283	90.147/90.147.11.30.05	48	19:07:33.617	1.784

2.3 CALCULATION OF COHERENCY

The spatial variability of the ground motion waveforms can be quantified by the spatial coherency. Let $u_j(t)$ be a recorded ground motion at location j. A window, v(t), is applied to $u_j(t)$ that picks out the largest shaking as described in Section 2.2. Here, we used a time window given by a 5% cosine bell.

$$v(t)=\begin{cases} 0.5\left[\cos\left(\dfrac{t\pi}{0.05W_L}+\pi\right)+1\right] & for\, t < 0.05W_L \\ 1 & for\, 0.05W_L \le 0.95W_L \\ 0.5\left[\cos\left(\dfrac{\pi(t-0.95W_L)}{0.05W_L}\right)+1\right] & for\, t > 0.95W_L \end{cases} \tag{2-2}$$

where W_L is the length of the time window, discussed in Section 2.2. The results are not sensitive to the shape of the time window used because the variability in the computed coherency between stations, events, and arrays is much larger than the differences due to the shape of the time window.

Let $u_j(\omega)$ be the Fourier transform of the windowed time series, $u_j(t)v(t)$, then

$$u_j(\omega) = \sum_{k=1}^{T} v(t_k)u_j(t_k)\exp(-i\omega t_k) \tag{2-3}$$

where T is the number of time samples, t_k is the time of the k^{th} sample, and ω is the frequency. The smoothed cross-spectrum is given by

$$S_{jk}(\omega) = \sum_{m=-M}^{M} a_m u_j(\omega_m)\overline{u}_k(\omega_m) \tag{2-4}$$

where 2M+1 is the number of discrete frequencies smoothed, $\omega_m=\omega+2\pi m/T$, a_m are the weights used in the frequency smoothing (the weights are discussed below), and the overbar indicates the complex conjugate. The coherency, $\gamma_{ij}(\omega)$, is given by

$$\gamma_{ij}(\omega) = \frac{S_{ij}(\omega)}{S_{ii}(\omega)S_{jj}(\omega)} \tag{2-5}$$

where $S_{ij}(\omega)$ is the smoothed cross-spectrum for stations i and j. As shown in Eq. 2-5, the coherency is a complex number. It is common to use the absolute value of the coherency (sometimes called the lagged coherency because it lags one ground motion with respect to the other ground motion to remove the phase shift due to wave-passage effect). A $Tanh^{-1}$ transformation is often applied to the lagged coherency to produce approximately normally distributed data (Enochson and Goodman, 1965). That is, the $Tanh^{-1}$ ($|\gamma|$) will be approximately normally distributed about the median $Tanh^{-1}(|\gamma|)$ curve. This is a well-known transformation used in time series analysis.

There are several ways the coherency can be described: lagged coherency, plane-wave coherency, and unlagged coherency. These three measures of coherency are described below.

2.3.1 Lagged Coherency

The lagged coherency is the most commonly cited coherency measure. It is the coherency measured after aligning the time series using the time lag that leads to the largest correlation of the two ground motions. It is given by $|\gamma|$. There is no requirement that the time lags be consistent between frequencies. In general, the lagged coherency does not go to zero at large separations and high frequencies due to the bias in the estimate of the lagged coherency. The level depends on the number of frequencies smoothed.

2.3.1 Plane-Wave Coherency

The plane-wave coherency differs from the lagged coherency in that it uses a single time lag for all frequencies. That is, it measures the coherency relative to a single wave speed for each earthquake. As a result, the plane-wave coherency is smaller than the lagged coherency. The plane-wave coherency is found by taking the real part of the smoothed cross-spectrum after aligning the ground motions on the best plane-wave speed. The plane–wave coherency will approach zero at high frequencies and large separations. It is unbiased.

2.3.1 Unlagged Coherency

The unlagged coherency measures the coherency assuming no time lag between locations. This corresponds to the assumption of vertical wave propagation. The unlagged coherency is given by the real part of the smoothed cross-spectrum. The unlagged coherency will be smaller than the plane-wave coherency. The unlagged coherency is found by multiplying the plane-wave coherency by $\cos(2\pi f \xi_R s)$ where f is the frequency, ξ_R is the separation distance in the direction of wave propagation, and s is the wave slowness (inverse of the apparent velocity). The coherent part of the wave passage effect can lead to negative values of the unlagged coherency. Negative values indicate that the ground motion at the two stations are out of phase. An unlagged coherency of –1 indicates that the ground motion is 180 degrees out of phase due to wave passage effects. For foundation dimensions of a few hundred meters of less, the travel time across the foundation is very small so wave passage effects are not significant. It is unbiased.

2.4 WAVE SPEEDS

In this study, we use the plane wave coherency. To compute the plane wave coherency, the wave speeds are required. The wave speeds were computed using the coherencies in the frequency band of 5-25 Hz. The resulting slownesses are listed in Table 2.

Table 2. Slowness Used For The Plane-Wave Coherency

Event Number	X Slowness (sec/km)	Y Slowness (sec/km)
1	0.4	0.1
2	0.0	-1.0
3	1.0	-0.3
4	0.2	-0.1
5	0.0	0.2
6	0.2	0.0
7	0.2	0.2
8	0.0	0.2
9	0.0	0.2
10	0.2	0.0
11	-0.1	0.3
12	0.2	0.0
13	0.0	0.2
26	-0.3	0.2
29	0.1	0.1
30	0.0	0.3
32	0.1	0.2
33	0.1	0.2
39	0.1	0.2
44	0.0	0.3
61	0.0	0.2
63	0.0	0.3
65	0.0	0.2
67	0.0	0.3
68	0.2	0.0
69	-0.1	0.1
71	0.2	0.0
74	0.0	0.3
76	-0.1	-0.1
80	-0.1	-0.2
84	0.0	0.3
85	0.0	0.2
86	-0.1	0.2
88	-0.2	0.3
100	0.0	0.2
125	0.2	0.0
126	0.0	0.2

Table 2. Slowness Used For The Plane-Wave Coherency (cont.)

Event Number	X Slowness (sec/km)	Y Slowness (sec/km)
128	0.0	0.3
131	0.2	0.0
136	0.0	0.2
141	0.0	0.3
143	0.0	0.3
144	0.2	0.1
146	0.1	0.1
148	0.1	0.2
152	0.0	0.3
154	-0.1	0.2
156	0.0	0.3
161	-0.2	0.3
162	-0.1	-0.1
175	-0.2	0.2
180	-0.1	-1.0
184	0.2	-0.1
190	0.2	-0.1
192	0.1	0.2
195	0.0	0.2
196	0.0	0.2
199	0.0	0.2
200	0.0	0.2
204	-0.1	0.3
209	0.6	-0.6
211	-0.1	-0.1
213	-0.1	0.3
215	0.0	0.2
226	-0.1	-0.1
234	0.0	0.2
236	0.2	0.0
237	0.0	0.3
243	0.0	0.2
245	-0.2	0.2
250	0.1	0.2
251	0.1	0.2
252	0.5	0.4
260	-0.1	0.2
270	-0.1	-0.2
271	0.0	-0.6
274	-0.1	-0.1
283	-0.1	-0.1

2.5 BINNING COHERENCIES

Using the 78 selected earthquakes, there are over 95,000 coherency pairs at each frequency. To reduce the number of coherency values to a manageable number for the regression analysis, the computed coherencies for each earthquake were put into 10 m distance bins (e.g. 0-10 m, 10-20m, …). The mean $\tanh^{-1}(\gamma_{pw}(f))$ was then computed for each frequency for each earthquake. In the averaging, the coherency values greater than 0.99 or less than -0.99 were set at 0.99 and -0.99, respectively to avoid large outliers (The $\tanh^{-1}$ transformation leads to infinite values as the coherency becomes 1 or -1, but the differences between coherency of 0.99 and 1.0 are of no practical importance.) The mean values were then used in the regression analysis described in Section 3.

3 Coherency Model

3.1 REGRESSION ANALYSIS

The plane-wave coherency is modeled by the following functional form:

$$\gamma_{pw}(f,\xi) = \left[1 + \left(\frac{f \;\; Tanh(a_3\xi)}{a_1 f_c(\xi)}\right)^{n1(\xi)}\right]^{-1/2} \left[1 + \left(\frac{f \;\; Tanh(a_3\xi)}{a_2}\right)^{n2}\right]^{-1/2} \tag{3-1}$$

The regression analysis was conducted using the $\tanh^{-1}(\gamma_{pw})$ because this transformation leads to residuals that are approximately normally distributed. The results are presented in terms of the untransformed coherency because it is easier to understand.

The coefficients were derived from using data from the 78 earthquakes listed in Table 1. Since most of the data were from small magnitude earthquakes with small amplitudes at the low frequencies, the computed coherencies are used only for freq > 5 Hz. The resulting model coefficients are given in Tables 3 and 4 for the horizontal and vertical components, respectively. The plane-wave coherency models for the horizontal and vertical components are shown in Figures 6 and 7, respectively.

3.2 RESIDUALS

The residuals for the horizontal and vertical coherencies are shown in Figures 8a,b and 9a,b. In these figures, each point is the residual of the mean coherency for the distance bin for one earthquake and one frequency. The mean residual over the frequency band of 10-35 Hz is shown in Figure 10. The model has near zero mean residual over the frequency band of 10-35 Hz.

Table 2. Plane-Wave Coherency Model Coefficients For The Horizontal Component

Coeff	Horiz Coeff
a_1	1.0
a_2	40
a_3	0.4
$n_1(\xi)$	$3.80-0.040*\ln(\xi+1)+0.0105[\ln((\xi+1)-3.6]^2$
n_2	16.4
$f_c(\xi)$	$27.9-4.82*\ln(\xi+1)+1.24[\ln((\xi+1)-3.6]^2$

Table 3. Plane-Wave Coherency Model Coefficients For The Vertical Component

Coeff	Vertical Coeff
a_1	1.0
a_2	200
a_3	0.4
$n_1(\xi)$	$2.03+0.41*\ln(\xi+1)-0.078[\ln((\xi+1)-3.6]^2$
n_2	10
$f_c(\xi)$	$29.2-5.20*\ln(\xi+1)+1.45[\ln((\xi+1)-3.6]^2$

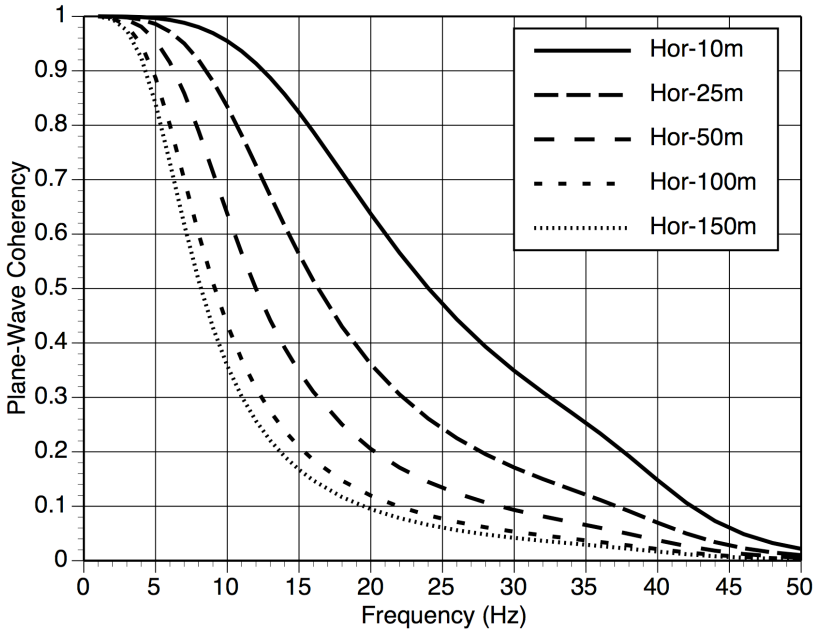

Figure 6. Plane-wave coherency for the horizontal component

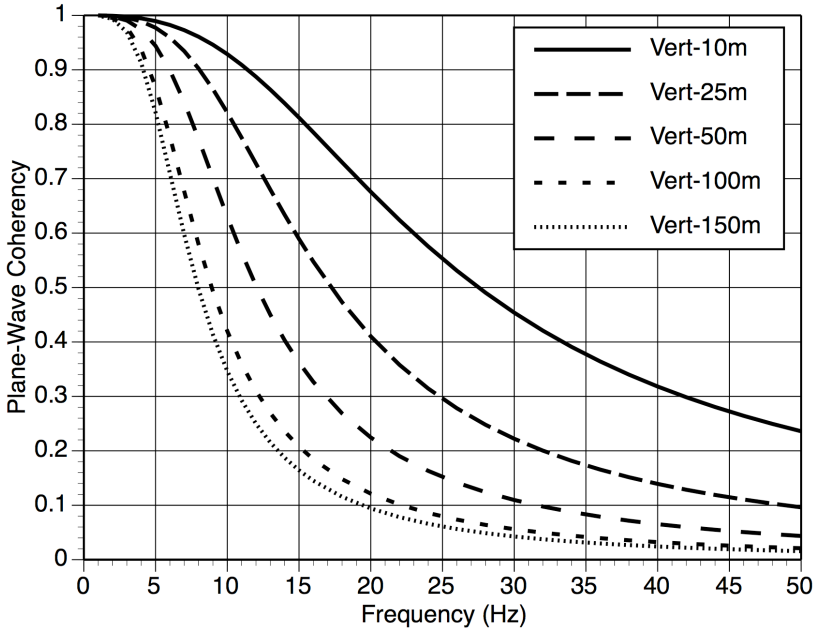

Figure 7. Plane-wave coherency for the vertical component

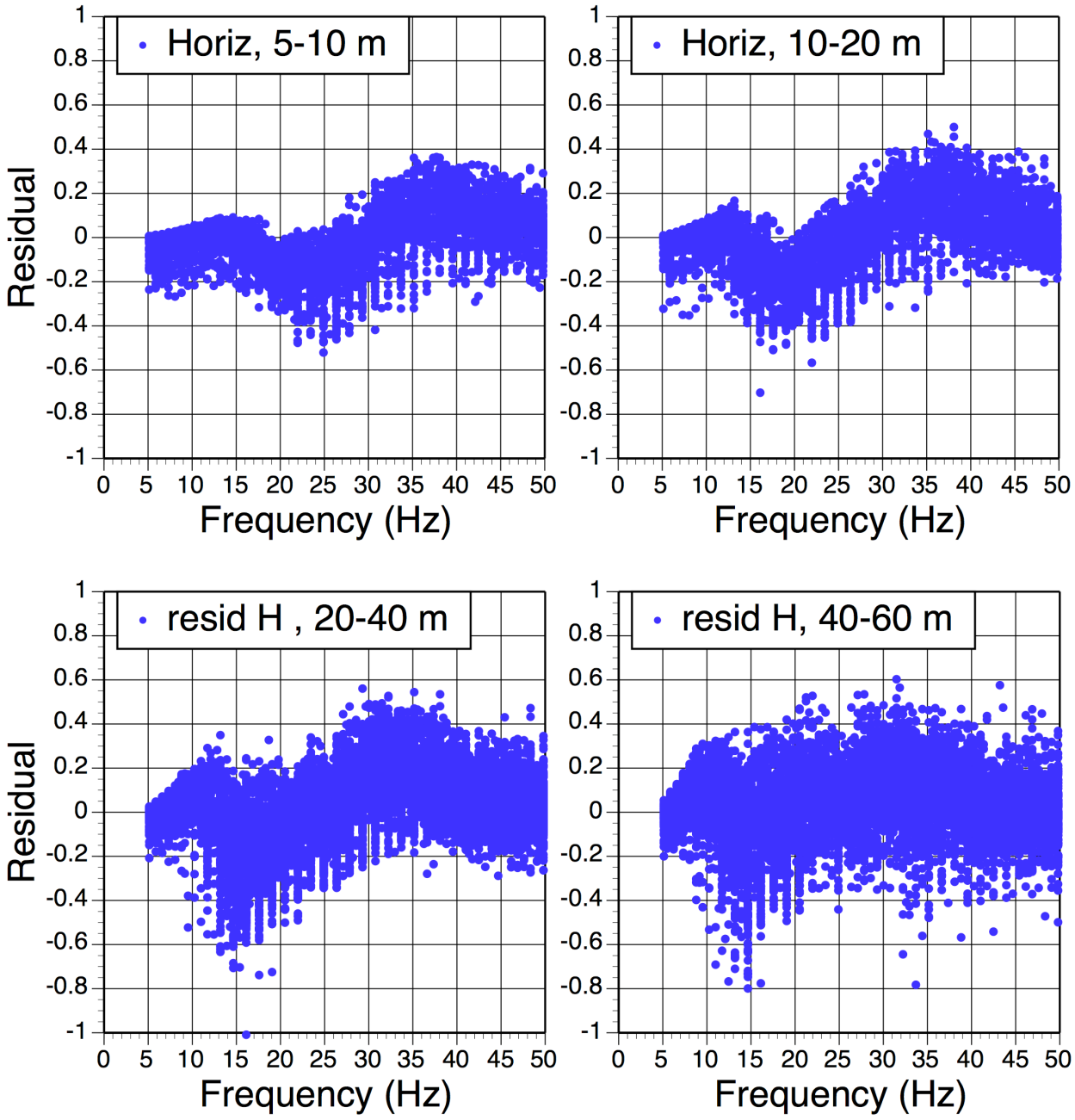

Figure 8a. Plane-wave coherency residuals for the horizontal component (separation distances of 5-60m)

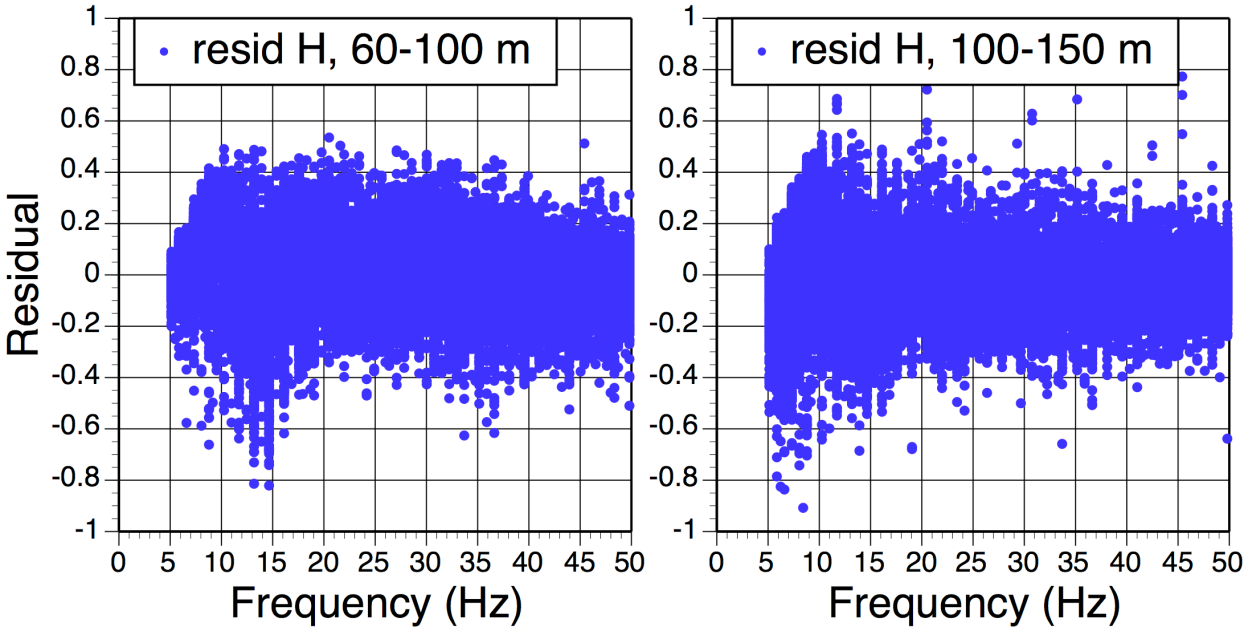

Figure 8b. Plane-wave coherency residuals for the horizontal component (separation distances of 60-150m)

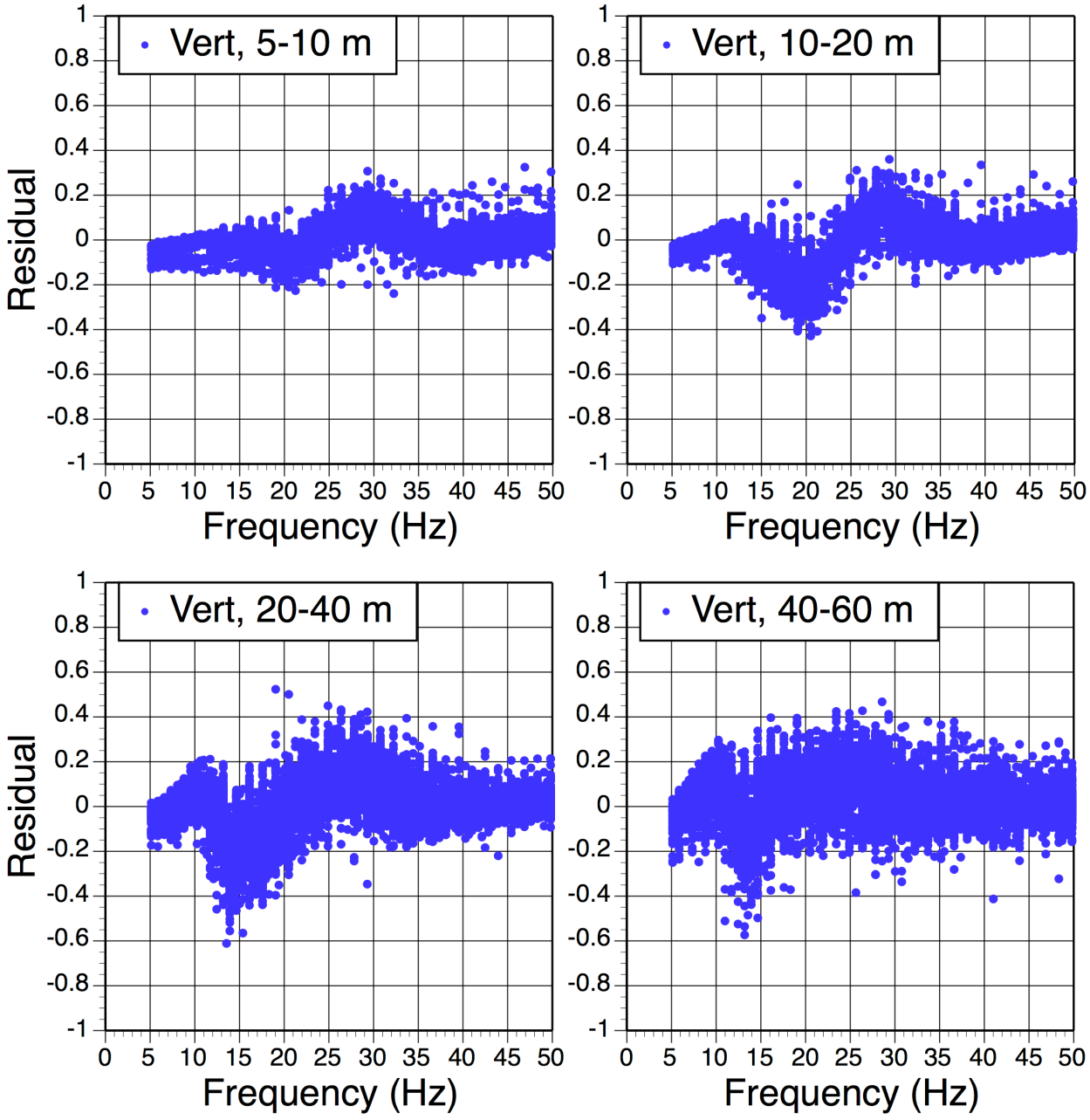

Figure 9a. Plane-wave coherency residuals for the vertical component (separation distances of 5-60m)

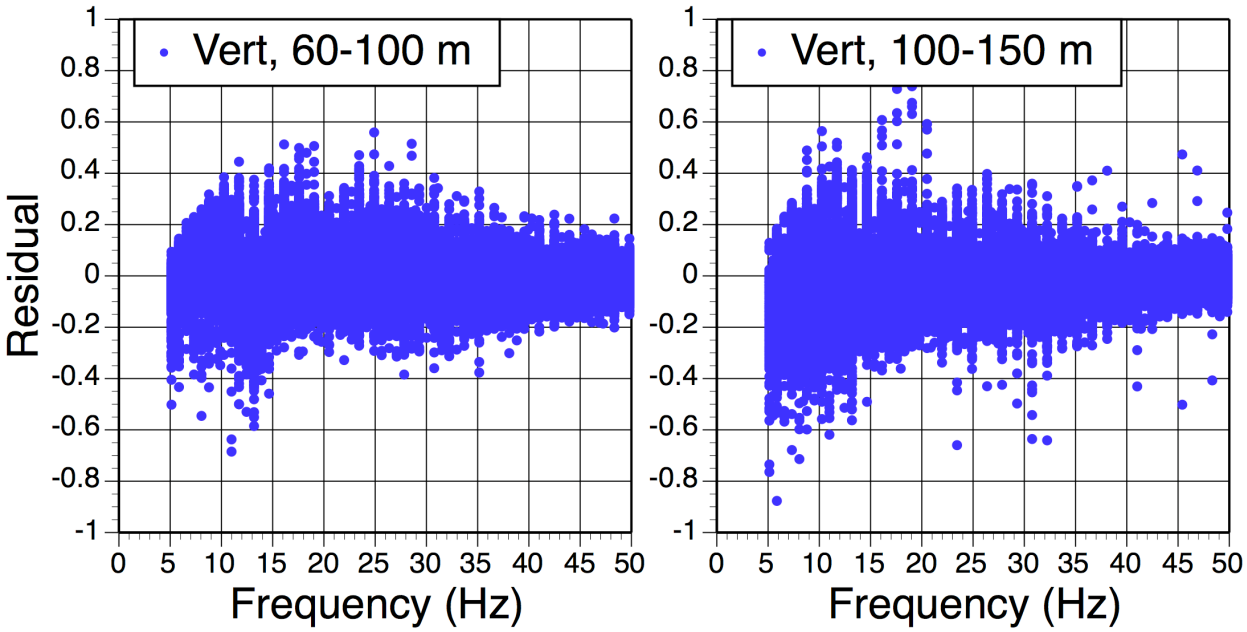

Figure 9b. Plane-wave coherency residuals for the vertical component (separation distances of 60-150m)

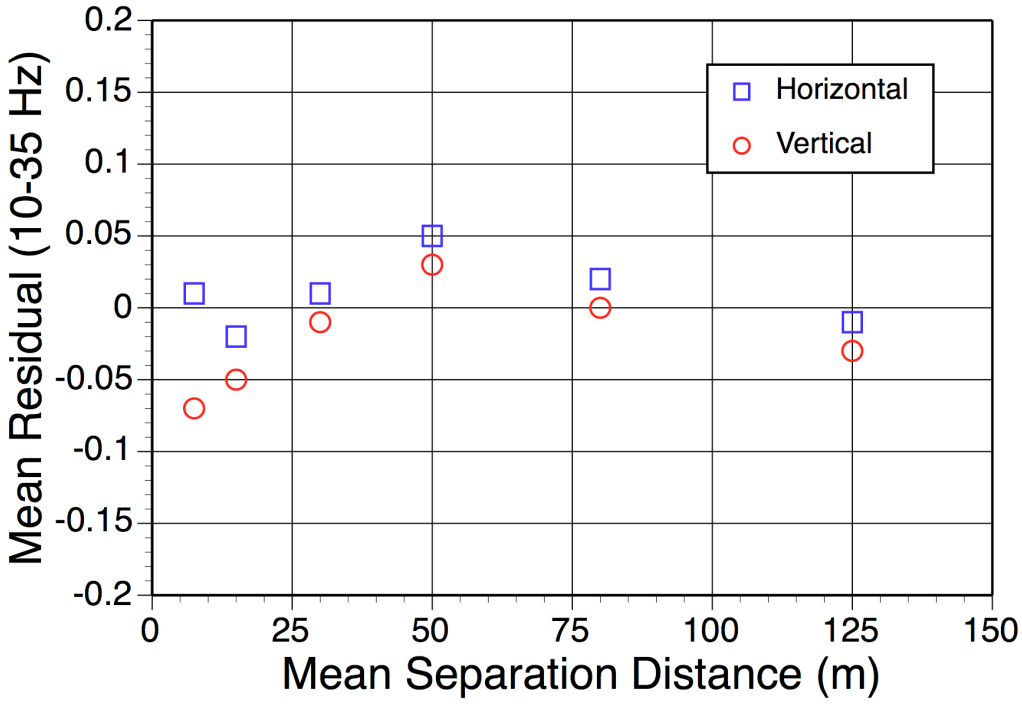

Figure 10. Mean residuals over 10-35 Hz.

References

Abrahamson, N. A. (2006). Program on Technology Innovation: Spatial Coherency Models for Soil-Structure Interaction. EPRI, Palo Alto, CA, and U.S. Department of Energy, Washington, DC: 2006. 1012968.

Enochson, L. D. and N. R. Goodman (1965). Gaussian approximations to the distribution of sample coherence, Tech Rep. AFFDL-TR-65-57, Wright-Patterson Air Force Base.

Louie, J. N., R. E. Abbott, and S. Pullammanappallil (2002). Refraction microtremor and optimization methods as alternatives to horeholes for site strength and earthquake hazard assessment, http://www.seismo.unr.edu/ftp/pub/louie/papers/louie-sageep02.pdf

Owens, T. J., P. N. Anderson, and D. E. McNamara (1991). The 1990 Pinyon Flat high frequency array experiment, An IRIS Eurasian seismic studies program passive source experiment, PASSCAL Data Report #91-002.

Vernon, F., L., G. L. Pavlis, T. J. Owens, D. E. McNamara, and P. N. Anderson, Near-Surface Scattering Effects Observed with a High-Frequency Phased Array at Pinyon Flats, California, Bull. Seism. Soc. Am., 88, 1548-1560.